https://ntrs.nasa.gov/search.jsp?R=20160006009 2019-08-31T03:02:17+00:00Z

Characterization of Flap Edge Noise Radiation from a High-Fidelity Airframe Model

William M. Humphreys, Jr.*, Mehdi R. Khorrami†, David P. Lockard‡,
Dan H. Neuhart§, Christopher J. Bahr¶
NASA Langley Research Center
Hampton, Virginia 23681-2199

The results of an experimental study of the noise generated by a baseline high-fidelity airframe model are presented. The test campaign was conducted in the open-jet test section of the NASA Langley 14- by 22-foot Subsonic Tunnel on an 18%-scale, semi-span Gulfstream airframe model incorporating a trailing edge flap and main landing gear. Unsteady surface pressure measurements were obtained from a series of sensors positioned along the two flap edges, and far field acoustic measurements were obtained using a 97-microphone phased array that viewed the pressure side of the airframe. The DAMAS array deconvolution method was employed to determine the locations and strengths of relevant noise sources in the vicinity of the flap edges and the landing gear. A Coherent Output Power (COP) spectral method was used to couple the unsteady surface pressures measured along the flap edges with the phased array output. The results indicate that outboard flap edge noise is dominated by the flap bulb seal cavity with very strong COP coherence over an approximate model-scale frequency range of 1 to 5 kHz observed between the array output and those unsteady pressure sensors nearest the aft end of the cavity. An examination of experimental COP spectra for the inboard flap proved inconclusive, most likely due to a combination of coherence loss caused by decorrelation of acoustic waves propagating through the thick wind tunnel shear layer and contamination of the spectra by tunnel background noise at lower frequencies. Directivity measurements obtained from integration of DAMAS pressure-squared values over defined geometric zones around the model show that the baseline flap and landing gear are only moderately directional as a function of polar emission angle.

Nomenclature

a_m	= shear layer amplitude correction	$P(f,T)$	= FFT of pressure time history for frequency f and block T
$\hat{A}$	= deconvolution influence matrix	$\hat{W}$	= microphone weight diagonal matrix
c	= flap chord length	$\hat{X}$	= deconvolved array output power vector
$COPs$	= coherent output power spectrum	$\hat{x}_m$	= distance from microphone to grid point
$\hat{e}$	= column vector with elements e_m	$\hat{Y}$	= array output power vector (elements $Y(\hat{e})$)
$\hat{G}$	= cross spectral matrix	w_m	= frequency-dependent microphone weight
G	= single channel auto-spectrum	γ_{as}	= COP coherence
G_a	= array output auto-spectrum	τ_{as}	= COP time delay from sensor to array
G_{as}	= array/pressure sensor cross spectrum	φ_{as}	= COP phase
k,m,n	= indices	Φ	= array tunnel station
$\hat{k}$	= wavenumber	θ_e, ξ_e	= polar and azimuthal emission angles
K	= number of FFT blocks	$\omega\Delta t$	= shear layer phase correction for frequency ω
M,N	= number of microphones, pressure sensors	ω_s	= window weighting constant

*Aerospace Engineer, Advanced Measurements and Data Systems Branch, Associate Fellow AIAA
†Aerospace Engineer, Computational AeroSciences Branch, Associate Fellow AIAA
‡Aerospace Engineer, Computational AeroSciences Branch, Senior Member AIAA
§Aerospace Engineer, Flow Physics and Control Branch
¶Aerospace Engineer, Aeroacoustics Branch, Senior Member AIAA

I. Introduction

The NASA Aeronautics Research Mission Directorate's Integrated Aviation Systems Program includes in its portfolio the Environmentally Responsible Aviation (ERA) Project. The goal of the ERA Project is to explore vehicle concepts and technologies that improve fuel efficiencies, reduce noise levels, and decrease harmful emissions for both the current and future fleet of aircraft traversing the national air transportation system.[1] The ERA project has among its goals the reduction of aircraft noise by 42 cumulative EPNL dB below Stage 4. Methods to achieve this include the reduction of flap and landing gear noise. This reduction requires a synergistic experimental assessment of the baseline noise generated by unmodified high lift and undercarriage structures, coupled with high fidelity numerical simulations of the flow-induced noise mechanisms on these structures. An understanding of the noise generation mechanisms can then drive the development and deployment of practical and effective noise mitigation concepts.

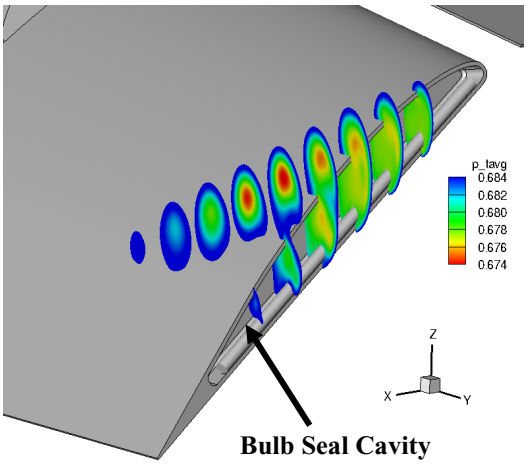

Figure 1. Time-averaged static pressure contours for a high-lift outboard flap side edge with a cavity for a bulb seal, highlighting flow-cavity interaction and vortex cores. From Ref. 11.

Over the past two decades a number of experimental and computational studies have been performed to understand and model the noise generated by the high lift flap side edge.[2-11] These studies have confirmed that a dual vortex system is present for a number of flap geometries such as the one shown in Figure 1, where a cavity is present at the flap edge to accommodate a bulb seal that aids in the mating process when the flap is retracted. The stronger of the two vortices in Fig. 1 is generated within the cavity and a weaker one is present on the top surface of the flap. These two vortices eventually merge and strengthen downstream. The large-scale flow fluctuations (and the resultant unsteady pressures at the flap side edge) associated with the shear layer roll-up, vortex formation, vortex merging, and the post-merged vortex instabilities are conjectured to be the main contributors to the noise radiation. Careful placement of unsteady pressure transducers at the flap edge can be used to verify the causality of the radiated noise. Coupled with far field acoustic measurements, a characterization of the noise radiation can be obtained. This was the goal of the current study, based on testing of an instrumented, 18%-scale, semi-span model of a Gulfstream aircraft installed in the NASA Langley 14- by 22-foot Subsonic Tunnel (14x22 tunnel) in the Spring of 2013. The tunnel test was performed as part of a larger airframe noise study executed under a NASA-Gulfstream partnership. An objective of the wind tunnel campaign was to characterize the nature of the flap side edge noise radiation by (1) identifying noise source regions on the model, (2) quantifying the noise

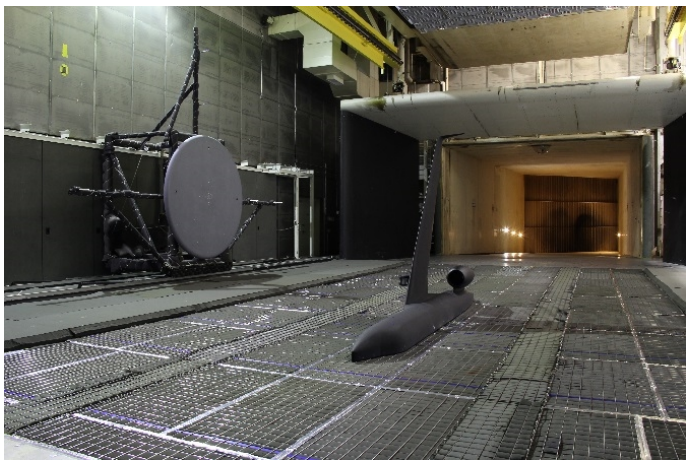

Figure 2. Phased array viewing pressure side of Gulfstream aircraft model, looking downstream in the 14x22 tunnel.

strength, (3) measuring the radiated noise directivity, and (4) coupling the fluctuating surface pressures with far field acoustic measurements. The characterization was conducted using a traversing microphone phased array mounted along the sidewall of the 14x22 tunnel test section viewing the pressure side of the model.[12] Figure 2 depicts the model and array installed in the 14x22 tunnel. The Unified DAMAS code (UDAMAS), which implements the DAMAS phased-array deconvolution method as described in Refs. 12 and 21, was used to obtain noise contour presentations and directivity for those sources present on the model. The array output was subsequently used in a Coherent Output Power (COP) method[7-8,13] that couples in the unsteady surface pressure signatures on the flap to obtain a measure of the apparent noise source distribution along the flap side edge. This paper presents a detailed characterization of the noise radiated by the flap system, including presentations of integrated spectra and directivity for the model with and without the main landing gear attached. The current study only addresses the baseline configuration of the model in the tunnel (no noise reduction components installed). A companion study looking at the effectiveness of noise reduction treatments is presented in Ref. 14.

II. Test Description

Tunnel: The 14- by 22-Foot Subsonic Tunnel is an atmospheric, closed-return tunnel that has the capability to test a variety of fixed and rotary wing aircraft and test articles, both powered and un-powered. The tunnel has a contraction area ratio of 9:1. Using a 12,000 horsepower drive system, the tunnel can generate airflows up to Mach 0.3, corresponding to a maximum Reynolds number of 2.2 x 10^6 per foot. The test section has dimensions of 14.5 feet high by 21.75 feet wide by 50 feet long and was configured for partial open-jet (floor in place) operation for the present study. For acoustic testing, the floor of the test section was lowered approximately 3 feet to permit the installation of rigid steel frame baskets containing sound absorbing acoustic foam wedges topped with 2-inch foam sheets (shown in Fig. 2). Additionally, foam sheets were applied to the floors outside of the test section. Acoustic foam wedges and perforated plates were attached to the raised ceiling and outer sidewalls of the test section. When combined with the floor baskets, these treatments created an effective semi-anechoic environment in the open-jet test section that minimized unwanted acoustic reflections.

Model: The model was a high-fidelity replica of a Gulfstream aircraft, designed and fabricated at NASA Langley using drawings provided by Gulfstream. The model was composed of a fuselage, wing, flap, flow-through nacelle, pylon, and main landing gear as shown in the exploded view in Figure 3. The length of the model was 185.4 inches with a wing span of 104.5 inches. It was designed such that a number of noise reduction treatments could be directly applied to the inboard and outboard flap edges and main landing gear. The model was highly instrumented with a total of 758 static pressure taps, 69 unsteady pressure transducers (40 of them on the flap), and 12 accelerometers. A detailed description of the model construction and instrumentation is provided in Refs. 15 and 16.

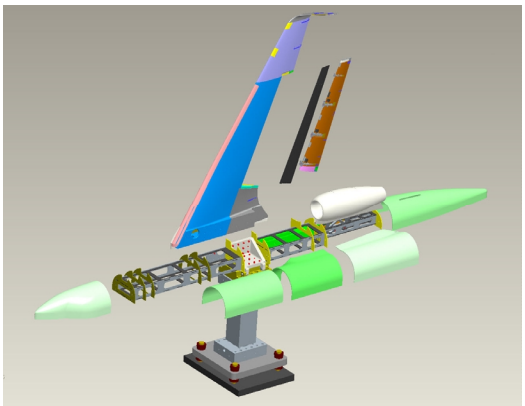

Figure 3. Gulfstream aircraft model - exploded view.

Unsteady Pressure Sensors: For this study, only those unsteady pressure transducers located along the upper surface of the outboard flap edge (Figure 4) and inboard flap edge (Figure 5) were used. The sensors were flush-mounted Kulite® differential unsteady pressure transducers†. Two different varieties of sensors were employed. The first consisted of model LQ-12A-062-2D sensors having a 0.04-inch opening diameter, a dynamic range of -2.0 psi to 0.6 psi, and a frequency range of 0 to 16 kHz. These sensors were

statically calibrated in situ over their operating range plus a 2% margin by applying the corresponding opposite-sign pressure to the reference side of the transducer. A highly-accurate reference pressure controller applied five test pressures over the calibration range and then a linear fit was applied to the DC signal to determine the sensitivity coefficients. The second variety of Kulite® sensors were model LQ-41-064-16A devices having a 0.025-inch opening diameter, a dynamic range of 0 psi to 16 psi, and a frequency range of 0 to 25 kHz. For these sensors, the manufacturer's published sensitivity coefficients were used. Table 1 summarizes the pressure sensors that were employed in the present study. The (x, y, z) coordinates for the sensors are given in tunnel coordinates referenced to the nozzle exit plane of the facility, assuming the model to be at a 3-degree angle of attack.

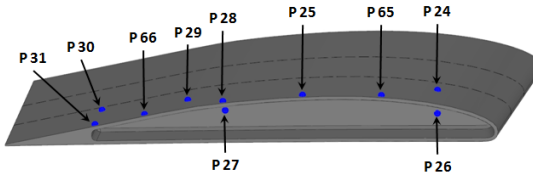

Figure 4. Positions and numbering of unsteady pressure transducers – flap outboard tip. From Ref. 16.

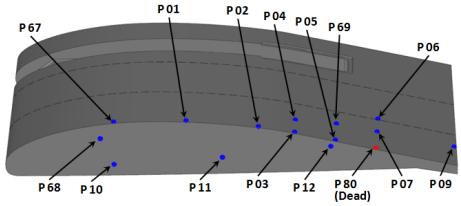

Figure 5. Positions and numbering of unsteady pressure transducers – flap inboard tip. From Ref. 16.

Table 1. Unsteady Pressure Sensors Utilized in Current Study

Sensor #	Type	Flap Edge	x location (inches)	y location (inches)	z location (inches)
P24	LQ-12A-062-2D	Outboard	248.66	71.70	-9.92
P65	LQ-41-064-16A	Outboard	249.25	72.06	-10.19
P25	LQ-12A-062-2D	Outboard	249.99	72.17	-10.71
P28	LQ-12A-062-2D	Outboard	250.69	72.29	-11.30
P29	LQ-12A-062-2D	Outboard	250.96	72.15	-11.62
P31	LQ-12A-062-2D	Outboard	251.71	72.51	-12.38
P67	LQ-41-064-16A	Inboard	234.82	20.41	-11.53
P01	LQ-12A-062-2D	Inboard	236.07	20.10	-12.53
P02	LQ-12A-062-2D	Inboard	237.20	19.82	-13.66
P03	LQ-12A-062-2D	Inboard	237.73	19.70	-14.28
P05	LQ-12A-062-2D	Inboard	238.29	19.57	-15.01

[†]Specific vendor and manufacturer names are explicitly mentioned only to accurately describe the test hardware. The use of vendor and manufacturer names does not imply an endorsement by the U.S. Government nor does it imply that the specified equipment is the best available.

Phased Array: The phased array incorporated 97 Bruel and Kjaer (B&K) Model 4938 1/4-inch pressure field microphones attached to Model 2670 1/4-inch preamplifiers powered by Model 5935L dual-channel conditioning supplies. Microphone signals were transmitted to the data acquisition system in the tunnel control room via LEMO microphone cables. The microphones were flush mounted (gap free) in a flat fiberglass honeycomb plate with total diameter of 8.05 feet. The array was designed for an operational frequency range of approximately 1.5 kHz to 80 kHz. This was achieved by using an irregular circular pattern of microphones comprised of 16 array arms with 6 microphones in each arm (see Figure 6). One microphone was positioned in the center of the array. The maximum array aperture size (outermost microphone to outermost microphone) was 78.6 inches, yielding a solid collecting angle of 21.2 degrees at a working distance of 17.5 feet from the array face to the center of the test section.[17] The array was attached to a rigid aluminum mounting frame that was in turn mounted to two parallel 44-foot linear traversing rails on the "south" side of the test section opposite the control room. The linear rails permitted the array face to traverse the majority of the length of the test section.

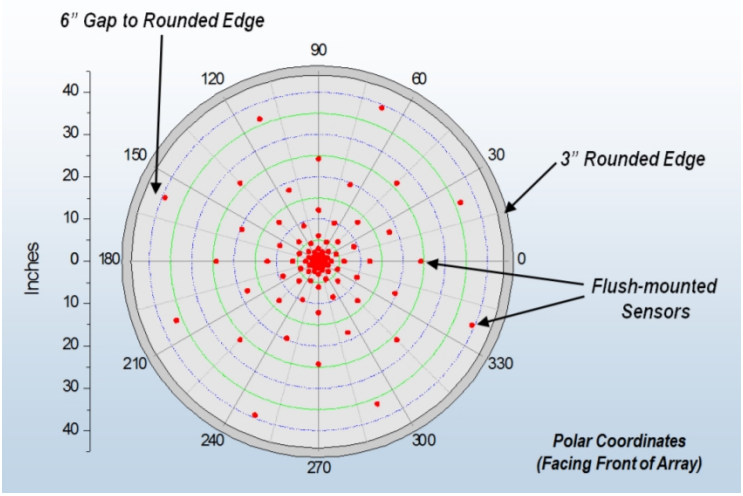

Figure 6. 14x22 tunnel phased array microphone pattern.

Data Acquisition: A highly distributed data acquisition system using commercially available hardware was assembled for this study. The data system had a total capacity of 192 channels and provided signal conditioning and digitization for both the phased array microphones and the model unsteady pressure transducers. A National Instruments Labview®-based program was developed and used for command and control of all of the hardware components of the data system as well as the linear traversing rails supporting the phased array. Acquired microphone and unsteady pressure transducer time history data were stored as a series of individual raw binary data files (one file per acquisition channel). The nominal acquisition window length was 30 seconds with a simultaneous sampling rate of 200 kHz used for all channels. The microphone signals were bandpass filtered from 400 Hz – 100 kHz. Additional details regarding the construction of the phased array and data acquisition system can be found in Ref. 12.

Data Reduction and Analysis: The reduction of data obtained from the array microphones and unsteady pressure transducers consisted of several steps:

1. The raw binary data files generated by the acquisition system were converted into Network Common Data Format (NetCDF) files[18] containing both the time history data and metadata regarding data acquisition settings, model parameters, and sensor calibrations.

2. For each test point, a hybrid Cross Spectral Matrix (CSM) was generated in engineering units for various combinations of phased array and unsteady pressure sensors, using as input the raw data NetCDF files generated in step 1. The CSM was partitioned between microphone and pressure sensor elements as follows:

$$\hat{G} = \begin{bmatrix} G_{a1a1} & G_{a1a2} & \cdots & G_{a1aM} & G_{a1s1} & G_{a1s2} & & G_{a1sN} \\ G_{a2a1} & \ddots & & \vdots & G_{a2s1} & \ddots & & \vdots \\ \vdots & & \ddots & \vdots & \vdots & & \ddots & \vdots \\ G_{aMa1} & \cdots & \cdots & G_{aMaM} & G_{aMs1} & \cdots & \cdots & G_{aMsN} \\ G_{s1a1} & G_{s1a2} & \cdots & G_{s1aM} & G_{s1s1} & G_{s1s2} & \cdots & G_{s1sN} \\ G_{s2a1} & \ddots & & \vdots & G_{s2s1} & \ddots & & \vdots \\ \vdots & & \ddots & \vdots & \vdots & & \ddots & \vdots \\ G_{sNa1} & \cdots & \cdots & G_{sNaM} & G_{sNs1} & \cdots & \cdots & G_{sNsN} \end{bmatrix} \quad (1)$$

where M is the total number of microphones in the array (extending from a_1 through a_M) and N is the total number of pressure sensors included in the analysis (extending from s_1 through s_N). The individual, block-averaged complex spectral elements are computed from

$$G_{mn}(f) = \frac{2}{K\omega_s T}\sum_{k=1}^{K}[P_{mk}^{*}(f,T)P_{nk}(f,T)] \quad (2)$$

where the frequency-domain pairs $P_m(f,T)$ and $P_n(f,T)$ are formed via Fast Fourier Transforms (FFT) of the corresponding pressure time histories. The time data are segmented into K non-overlapping blocks before the FFT is applied. ω_s represents a weighting constant to account for the Hamming window applied to the time history segments.

Both conventional background subtraction and a new subtraction technique based on eigenvalue decomposition of the background noise CSM as developed by Bahr et. al[19] were used to remove tunnel drive and circuit noise from the coherent output power spectral measurements.

3. Detailed analysis of the array data was performed using conventional frequency-domain delay and sum beamforming coupled with the DAMAS algorithm for generation of final noise source map presentations. For this, the upper left M by M quadrant of the CSM in Eqn. (1) is extracted to form $\hat{G}_{array}$ (representative of the CSM for the array in isolation):

$$\hat{G}_{array} = \begin{bmatrix} G_{m1m1} & G_{m1m2} & \cdots & G_{m1mM} \\ G_{m2m1} & \ddots & & \vdots \\ \vdots & & \ddots & \vdots \\ G_{mMm1} & \cdots & \cdots & G_{mMmM} \end{bmatrix} \quad (3)$$

The conventional beamformer summed output power takes the form of

$$Y(\hat{e}) = \frac{\hat{e}^T\hat{W}\,(\hat{G}_{array})_{diag=0}\,\hat{W}^T\hat{e}}{\left(\sum_{m=1}^{M} w_m\right)^2 - \sum_{m=1}^{M} w_m^2} \quad (4)$$

where w_m is a frequency-dependent weighting function designed to yield a pseudo-invariant array beamwidth over a broad frequency range spanning 2 – 30 kHz. $\hat{W}$ is a diagonal matrix containing the individual microphone weights. $\hat{e}$ is a column vector containing the individual steering values e_m:

$$e_m = a_m \frac{r_m}{r_c} exp\{j[(\hat{k}\cdot\hat{x}_m) + (\omega\Delta t_{m,shear})]\} \quad (5)$$

where $\hat{k}$ is the local wavenumber vector and $\hat{x}_m$ is the distance from the steering location to microphone m. The ratio (r_m/r_c) normalizes the amplitude, based on spherical spreading, to that of

the center microphone in the array at a distance of r_c. The phase correction $\omega\Delta t_m$ for microphone m accounts for the refraction of sound transmission through the open-jet shear layer. The amplitude correction a_m (including convective amplification) and phase correction are determined using Amiet's method.[20] For this study, the polar and azimuthal emission angles, θ_e and ξ_e, as determined from the shear layer corrections are defined in Figure 7.

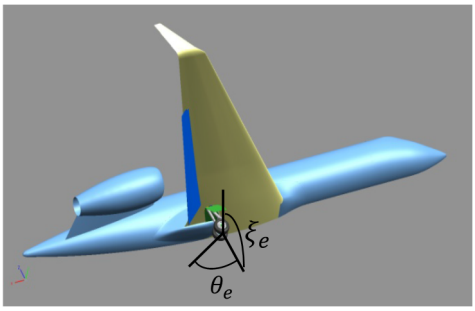

Figure 7. Polar and azimuthal emission angle definitions. θ_e = 0° is in the direction of flight. θ_e = 90°, ξ_e = 0° is the flyover location.

A parallelized version of DAMAS, called Unified DAMAS (UDAMAS, combining aspects of both the DAMAS and DAMAS-C algorithms) was executed on the NASA Langley mid-level compute capability K cluster. DAMAS performs a Point Spread Function (PSF) deconvolution of the array output via a Gauss-Seidel solution of the inverse problem

$$\hat{X} = \hat{A}^{-1}\hat{Y} \tag{6}$$

where $\hat{A}$ is an influence matrix representing the contributions of the PSF to the array output.[21] The result of solving Eqn. (6) is a deconvolved source distribution in $\hat{X}$. Beamformed ($\hat{Y}$) and deconvolved ($\hat{X}$) contour maps showing dB noise source presentations for standard 1/12-octave bands were generated during the analysis runs. Details of this are further described in Ref. 12.

4. A COP method similar to that used in Refs. 7, 8 and 13 was employed to obtain a measure of the noise source distribution along the flap edges, using the sensors shown in Figs. 4 and 5. The COP analysis relates the output of the unsteady pressure transducers on the model surface to the output of the phased array system. When the array is electronically steered to a specific pressure sensor location as defined in Table 1, the spectrum of the surface pressure sensor output that is coherent with the microphone array output can be computed via

$$COP_s = \frac{|G_{as}|^2}{G_a} = \gamma_{as}^2 G_s \tag{7}$$

where COP_s is the coherent output power spectrum, G_s is the pressure sensor auto spectrum, G_a is the auto-spectrum obtained from the output of the array, G_{as} is the cross-spectrum between the array and pressure sensor output, and γ_{as}^2 is the coherence. As described in Ref. 22, a data block time-shifting method was used to avoid time-delay bias errors that occur due to the physical propagation of the noise from the flap to the array (propagation time = τ_{as}) when using a common data acquisition time base. The microphone time histories were initially integer-shifted by an amount close to the value of τ_{as} during the generation of the CSM. The final adjustment to obtain the exact τ_{as} was performed in the frequency domain for the COP spectra via

$$(G_{as})_{\tau_{as}} = G_{as}e^{-j\omega\tau_{as}} \tag{8}$$

with the time-adjusted COP phase, $(\varphi_{as})_{\tau_{as}}$, represented as

$$(\varphi_{as})_{\tau_{as}} = \varphi_{as} - \omega\tau_{as} \tag{9}$$

These adjustments were determined taking into account the shear layer refraction effects in the tunnel.

III. Results and Discussion

For the current study, the angle of attack of the model was set to 3 degrees with a flap angle setting of 39 degrees. All data shown for this study were acquired at Mach 0.2 with the main landing gear both installed on the model and removed. The microphone array was positioned at a number of streamwise stations with respect to the center of the main landing gear truck (the defined reference location on the model). These stations spanned 60 to 110 degrees in 10 degree increments with an additional station at 54 degrees included in the test matrix (this was the farthest upstream that the array could be traversed in the tunnel test section). Table 2 summarizes the stations at which data were acquired along with the equivalent polar and azimuthal emission angles, using the convention noted in Fig. 7. Note that the azimuthal emission angles are invariant with array station due to the mounting of the array at a fixed height above the 14x22 tunnel test section floor (and thus above the centerline of the model fuselage).

Table 2. Array Measurement Locations and Emission Angles

Array Station Φ (degrees)	Array Streamwise Location (inches)	Polar Emission Angle θ_e (degrees)	Azimuthal Emission Angle ξ_e (degrees)
54	84.0	52.1	14.4
60	113.57	56.8	14.4
70	155.69	65.1	14.4
80	192.73	73.9	14.4
90	227.54	83.1	14.4
100	262.34	92.9	14.4
110	299.38	103.1	14.4

DAMAS Noise Source Distributions: Figures 8 through 10 depict DAMAS deconvolved source distribution maps showing the predominant flap and landing gear noise generation regions for 1/12-octave center frequencies of 5, 7.5, and 10 kHz, respectively. These three frequencies were chosen since they covered the range where the outboard flap bulb seal cavity was strongly resonant. The results are shown with CSM diagonal removal performed for 250 DAMAS Gauss-Seidel passes through the measurement grid, using four different sweep directions to minimize residual energy migration through the grid. Each figure contains 7 panels showing individual source distributions corresponding to the array stations and polar emission angles in Table 2. In each contour map, the dB levels have been normalized to the local peak level shown in that map. The noise radiation from the outboard flap edge with bulb seal cavity can be clearly identified in Figure 8 for mid-range polar angles from 56.8 to 83.1 degrees (Φ = 60 to 90 degrees). In contrast, the combination of the inboard flap edge and landing gear shows noise radiation across all of the polar angles. Given the proximity of the inboard flap and landing gear and the spatial resolution of the array, it is not possible to separate the noise generated by the flap from that caused by the gear in the figure. Similar trends can be seen in Fig. 9 for the 7.5-kHz center frequency, although the radiation from the outboard flap edge has shifted to be more pronounced at the higher polar angles. As shown in Fig. 10, this shift in directivity toward the higher angles continues for the 10-kHz center frequency. Also, the general appearance of the map degrades as the polar emission angle increases, with the greatest degradation shown for the 103.1-degree angle (Φ = 110 degrees). This is postulated to be caused by tunnel background noise, in particular scattering from the open-jet collector in the test section, but could also be partially caused by open-jet shear layer scattering in the facility since the shear layer thickens significantly as one moves downstream from the tunnel nozzle.

Figures 11 through 13 depict similar DAMAS deconvolved source maps for the case where the landing gear has been removed from the model, to better allow identification of inboard flap noise sources. The results are again shown for 1/12-octave frequencies of 5, 7.5, and 10 kHz for the stations and polar angles in Table 2. In Fig. 11 the outboard flap edge noise is somewhat similar in appearance to that shown in Fig. 8,

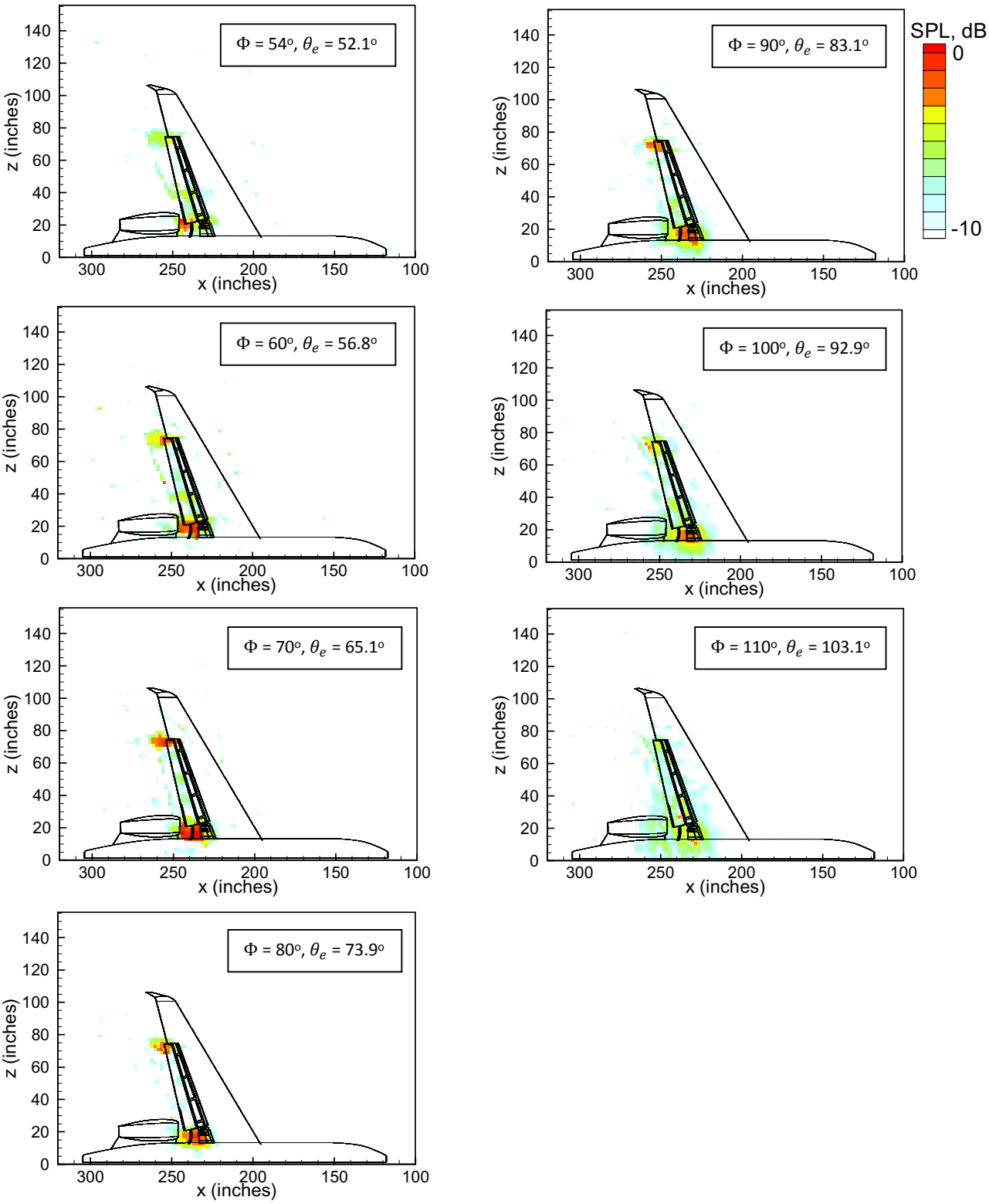

Figure 8. DAMAS noise source distributions. Baseline model with attached landing gear. Mach 0.2, AoA = 3°, Flap = 39°, $f_{1/12}$ = 5 kHz.

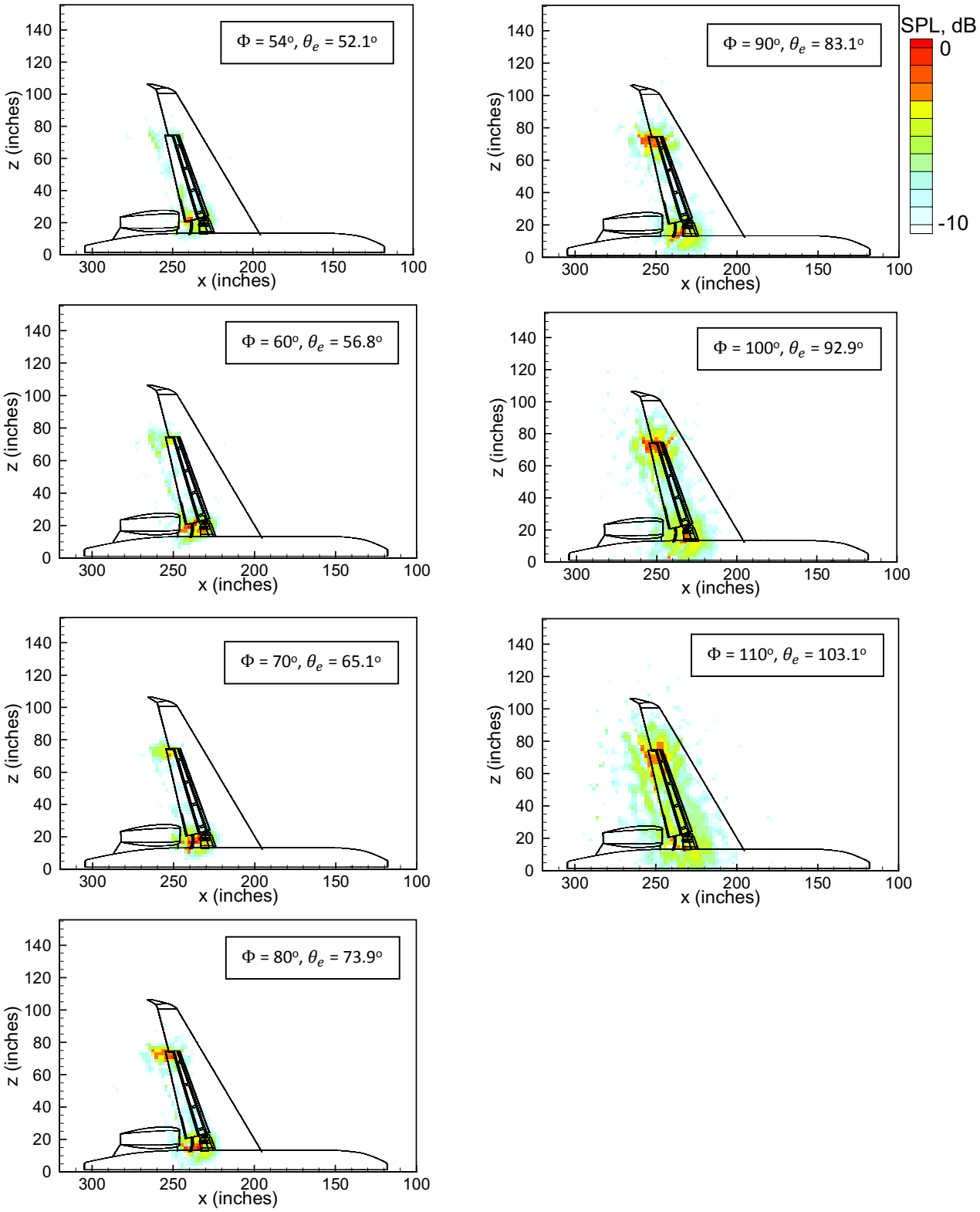

Figure 9. DAMAS noise source distributions. Baseline model with attached landing gear. Mach 0.2, AoA = 3°, Flap = 39°, $f_{1/12}$ = 7.5 kHz.

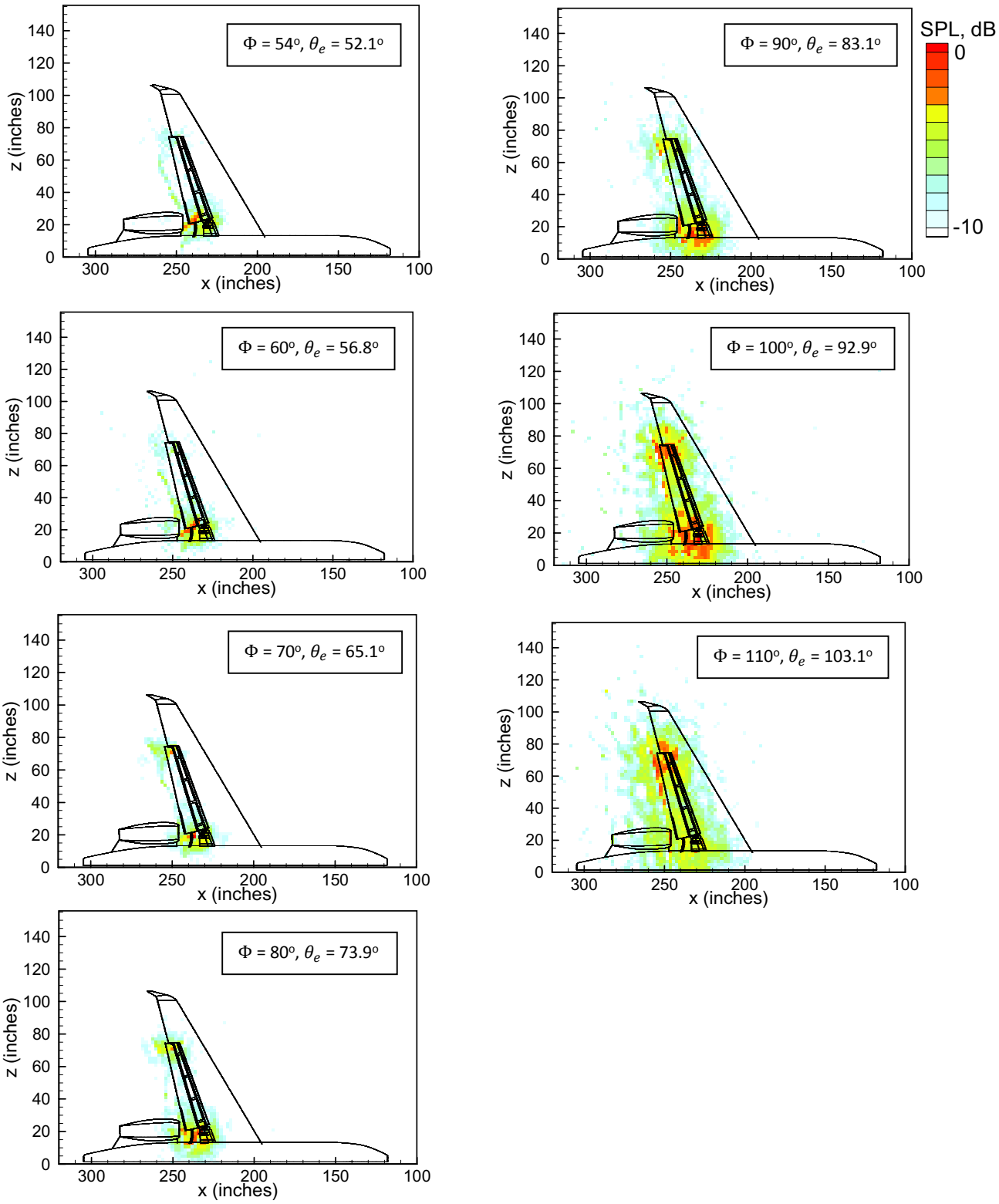

Figure 10. DAMAS noise source distributions. Baseline model with attached landing gear. Mach 0.2, AoA = 3°, Flap = 39°, $f_{1/12}$ = 10 kHz.

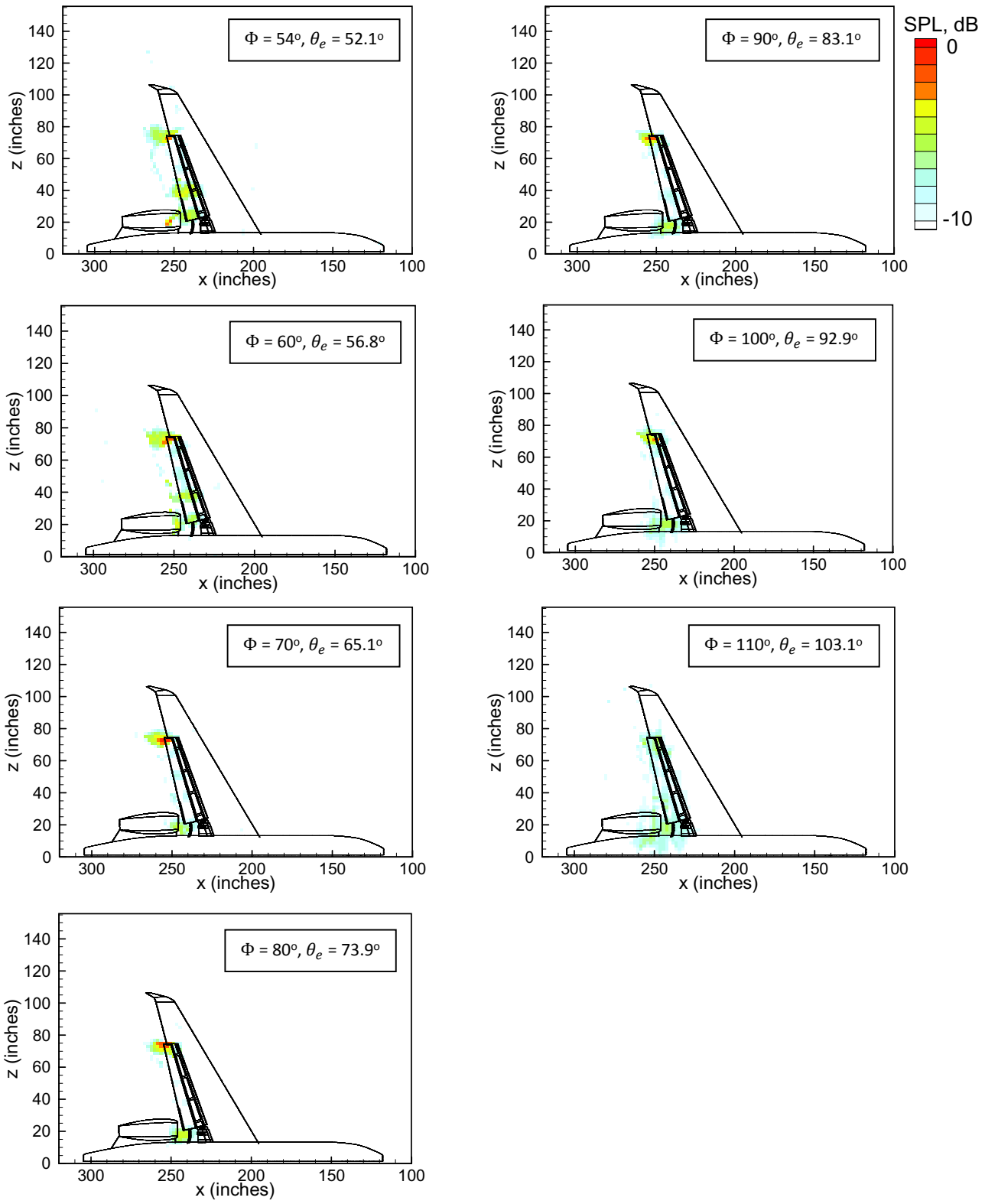

Figure 11. DAMAS noise source distributions. Baseline model – no landing gear. Mach 0.2, AoA = 3°, Flap = 39°, $f_{1/12}$ = 5 kHz.

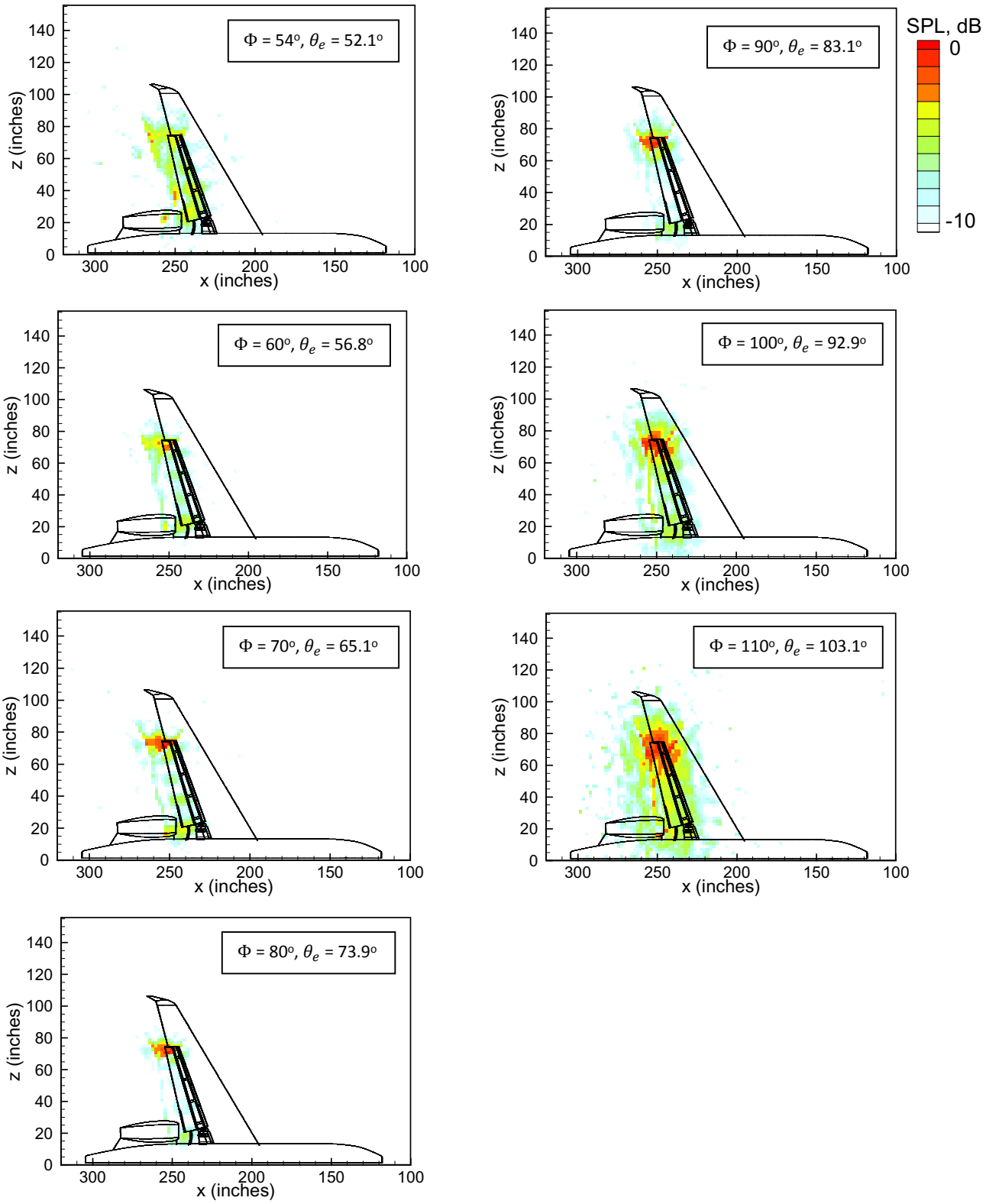

Figure 12. DAMAS noise source distributions. Baseline model – no landing gear. Mach 0.2, AoA = 3°, Flap = 39°, $f_{1/12}$ = 7.5 kHz.

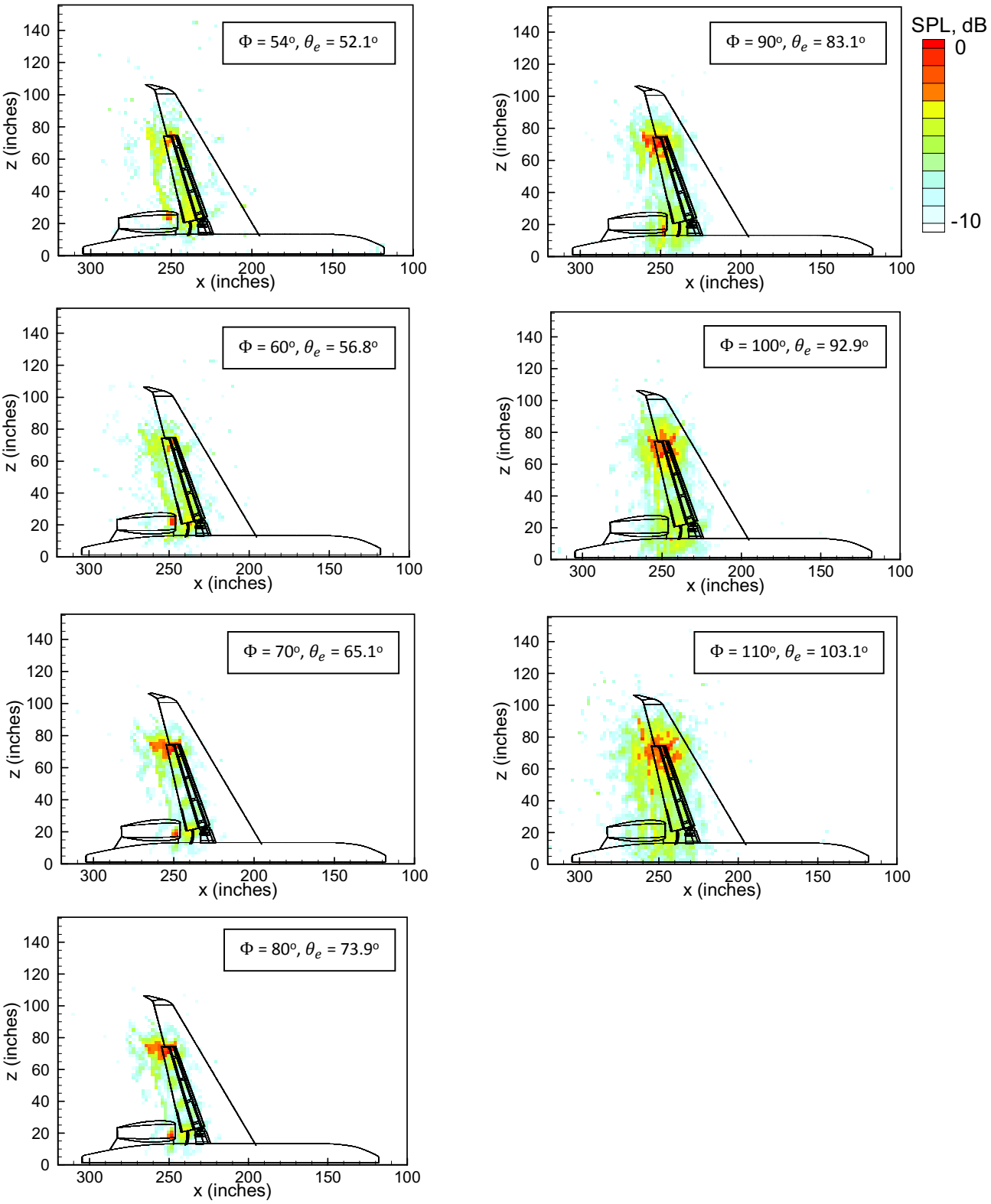

Figure 13. DAMAS noise source distributions. Baseline model – no landing gear. Mach 0.2, AoA = 3°, Flap = 39°, $f_{1/12}$ = 10 kHz.

as would be expected since removal of the landing gear should have only minimal influence on the outboard flap edge (the exception would be through modification of the swept flow along the wing). The noise distribution along the inboard flap edge is modified with removal of the gear, and there is only relatively weak noise radiation from the inboard edge at 5 kHz. The same is true for Fig. 12 where again the outboard edge dominates with much less radiation depicted from the inboard edge when plotted on the same dB scale. Comparisons of noise generation regions in Figs. 11 through 13 with like regions in Figs. 8 through 10 provide a strong indication that the noise observed around the inboard flap tip at frequencies greater than 5 kHz is strongly influenced by the landing gear. Finally, in Fig. 13 there appears to be a secondary noise source located in the vicinity of the flow-through nacelle for those polar angles from 52.1 to 83.1 degrees (Φ = 54 to 90 degrees). The cause of this particular sound source is not currently known with certainty.

Integrated Noise Spectra and Directivity: Figure 14 shows the spatial regions that were defined around the model in order to compute power spectral density (PSD, dB/Hz) integrated spectra for this study. Zone 1 represents integration of the entire measurement grid around the model and is used diagnostically to compare the DAMAS integrations with the auto-spectrum for array microphone 1 (the center microphone). Zone 2 represents integration of the combination of the inboard flap edge, landing gear and a portion of the flow-through nacelle. Zone 3 represents integration of the outboard flap edge and bulb-seal cavity. Finally, Zone 4 represents integration of the entire wing area. For each zone, the spectral levels were obtained on a narrowband basis (f = 171 Hz) by simple summing of the mean squared pressures generated by the DAMAS deconvolution over the region of interest. These were then converted to PSD's. All of the spectral data presented are based on model scale frequencies.

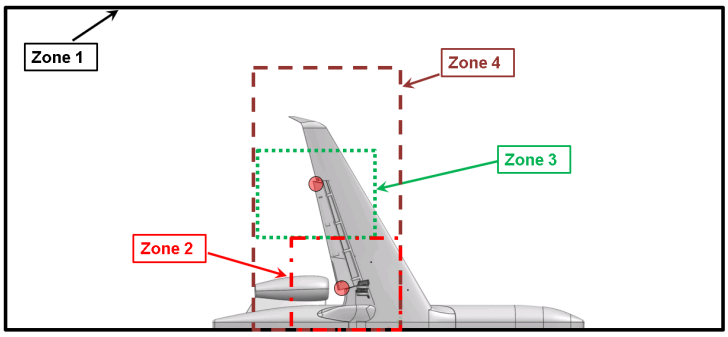

Figure 14. Defined spectral integration zones.

Figure 15 depicts the integrated noise spectra for the four zones shown in Fig. 14 plus the microphone 1 (array center) auto-spectrum for a polar emission angle of 92.9 degrees (Φ = 100 degrees, near the flyover

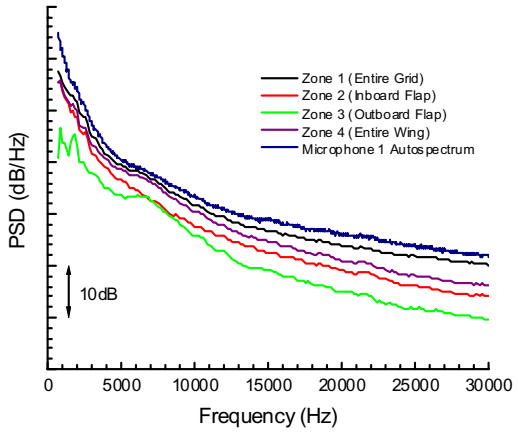

Figure 15. Integrated spectral signatures. Baseline model with landing gear. θ_e= 92.9°, Mach 0.2, AoA = 3°, Flap = 39°.

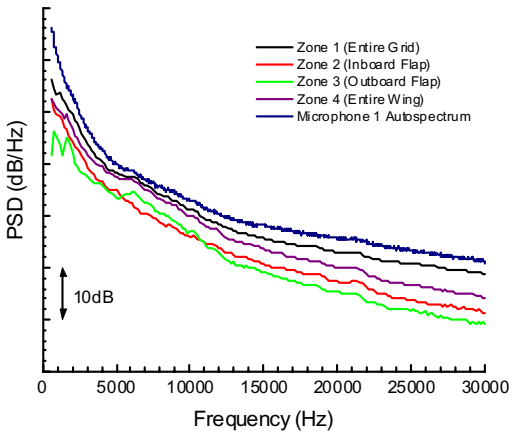

Figure 16. Integrated spectral signatures. Baseline model - no landing gear. θ_e= 92.9°, Mach 0.2, AoA = 3°, Flap = 39°.

point in emission coordinates) with the landing gear attached. The integrated spectra for each of the four zones are clearly distinct and separate in the figure.

There are three features shown in the spectra of Fig. 15 that are noted. The first is the comparison between the Zone 1 integration (the entire measurement grid) and the array microphone 1 auto-spectrum. Given that the Zone 1 integration should in theory capture all of the noise generated by the model, in an ideal setting this should equal the integrated noise captured by an individual microphone in the array. This has been demonstrated previously in studies of landing gear noise in anechoic facilities such as the NASA Langley Quiet Flow Facility.[23] However, in comparing the auto-spectrum for microphone 1 with that for Zone 1 in Fig. 15, there is a difference shown across all frequencies with an approximately 2-3 dB delta for frequencies above 7.5 kHz. It can be concluded that tunnel background noise is contributing to the single microphone spectra and that the DAMAS integrations are rejecting a portion of that noise. Unfortunately the corruption by facility background noise implies that single microphone spectra cannot be reliably utilized for directivity measures for this model in the 14x22 tunnel. The second feature that is noted from Fig. 15 is the broad peak in the Zone 3 (outboard flap edge) integrated spectra in the 5- to 10-kHz range, due to resonance from the bulb seal cavity spanning the entire chord of the flap. As will be shown subsequently in the COP analysis, this resonance results in the cavity being a strongly radiating source. It is noted that the spectral signatures shown in Fig. 15 are slightly different from the signatures observed in Refs. 14 and 15 for like model geometries, orientations and flow conditions. The majority of the acoustic data shown in these other studies were acquired using non-instrumented flap tips versus the unsteady pressure sensor-instrumented tips employed for the present study. There were subtle differences in the geometric characteristics of the bulb seal cavity (e.g., volume, wall thickness, bulb seal placement, small protrusions due to instrumentation, etc.) between the instrumented and non-instrumented tips. It is conjectured that these cavity differences are contributing to the modified spectral signature (in particular the cavity resonance) observed in the current spectra versus the legacy results.

Figure 16 shows similar integrated noise spectra to that shown in Fig. 15, but this time with the landing gear removed. The spectra are again displayed for a polar emission angle of 92.9 degrees ($\Phi = 100$ degrees). The overall structure of the integrated spectra is similar. The exception is that, with the elimination of the landing gear noise, Zone 3 now dominates over Zone 2 in the 5- to 10-kHz range due to the continued prominence of the outboard flap bulb seal cavity noise. Observe that the inboard flap edge generates more noise above 12 kHz versus the outboard flap edge than can be explained by the difference in the relative geometric scales (chord lengths) of the two flap edges. As explained in more detail in Ref. 14, cable bundle and bracket effects in the flap cove could be a possible cause. Finally, the integrated auto-spectrum for microphone 1 again exceeds the level for the Zone 1 integration by approximately 3 dB over a broad frequency range, showing that tunnel background noise (presumably) continues to contaminate the single microphone spectra.

By compiling the full range of integrated spectra like that shown in Figs. 15 and 16, the directivity of the model for the polar emission angles listed in Table 2 for each of the four defined integration zones can be created. This is shown in Figure 17 for the model with attached landing gear, and in Figure 18 for the model with the gear removed. An examination of the directivity for the various zones in each figure shows that in general there is only moderate directivity displayed for most of the noise sources on the model. In

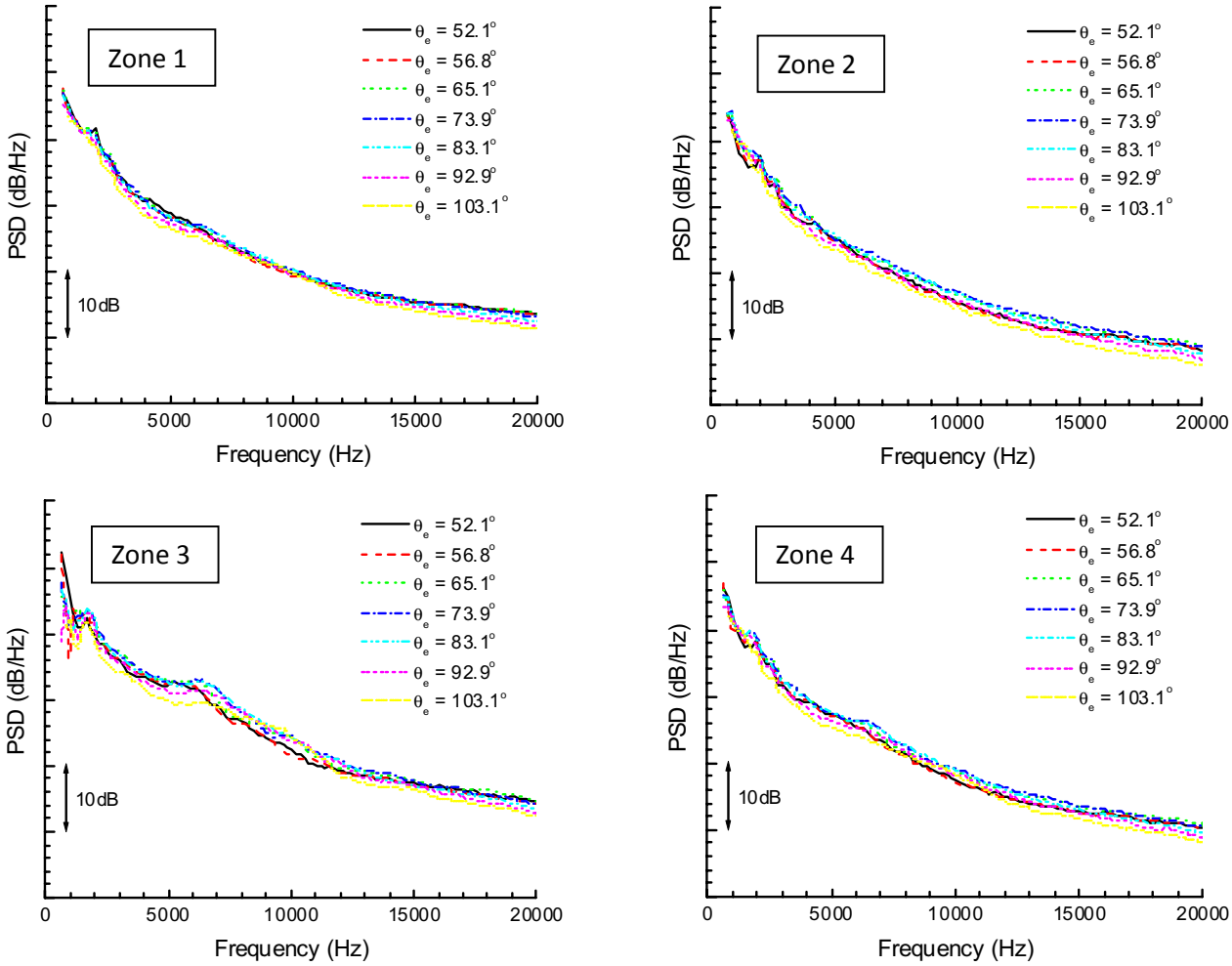

Figure 17. Directivity spectra for zones defined in Fig. 14. Baseline model with landing gear. Mach 0.2, AoA = 3°, Flap = 39°.

particular there is very little directivity depicted for Zone 1, but this is expected since integration of the entire measurement grid captures contributions from all noise sources on the model and thus averages out contributions from those sources. An examination of directivity for Zone 2 shows minimal variation with the landing gear installed (Fig. 17); however, there is a noticeable decrease in the dB levels (on the order 3 dB) at the lowest and highest polar emission angles when the landing gear is removed (Fig. 18). Regarding the outboard flap edge and bulb seal cavity (Zone 3), there is some directivity observed between 5 and 15 kHz with a spread of approximately 2-4 dB between the 52.1-degree and 92.9-degree polar angles. The directivity for Zone 4 is somewhat similar to that for Zone 1 since integration of the entire wing again averages contributions from different sources.

COP Analysis of Flap Edge Noise Distributions: Figure 19 depicts the results of a typical COP analysis. For this example, the landing gear was installed on the model, and the array was positioned at Φ = 100 degrees (θ_e = 92.9 degrees) and steered to unsteady pressure sensor P31 on the outboard flap. Shown are four individual power spectral densities ($\Delta f = 1\ Hz$) for the pressure sensor auto-spectrum (G_s), the array auto-spectrum (G_a), the cross-spectrum between the array and the pressure sensor (G_{as}), and the coherent output power spectrum (COP_s). Along with these are shown the coherence between the array and the pressure sensor (γ_{as}^2), and the cross spectral phase ($\varphi_{as} - \omega\tau_{as}$) associated with the COP_s. For this

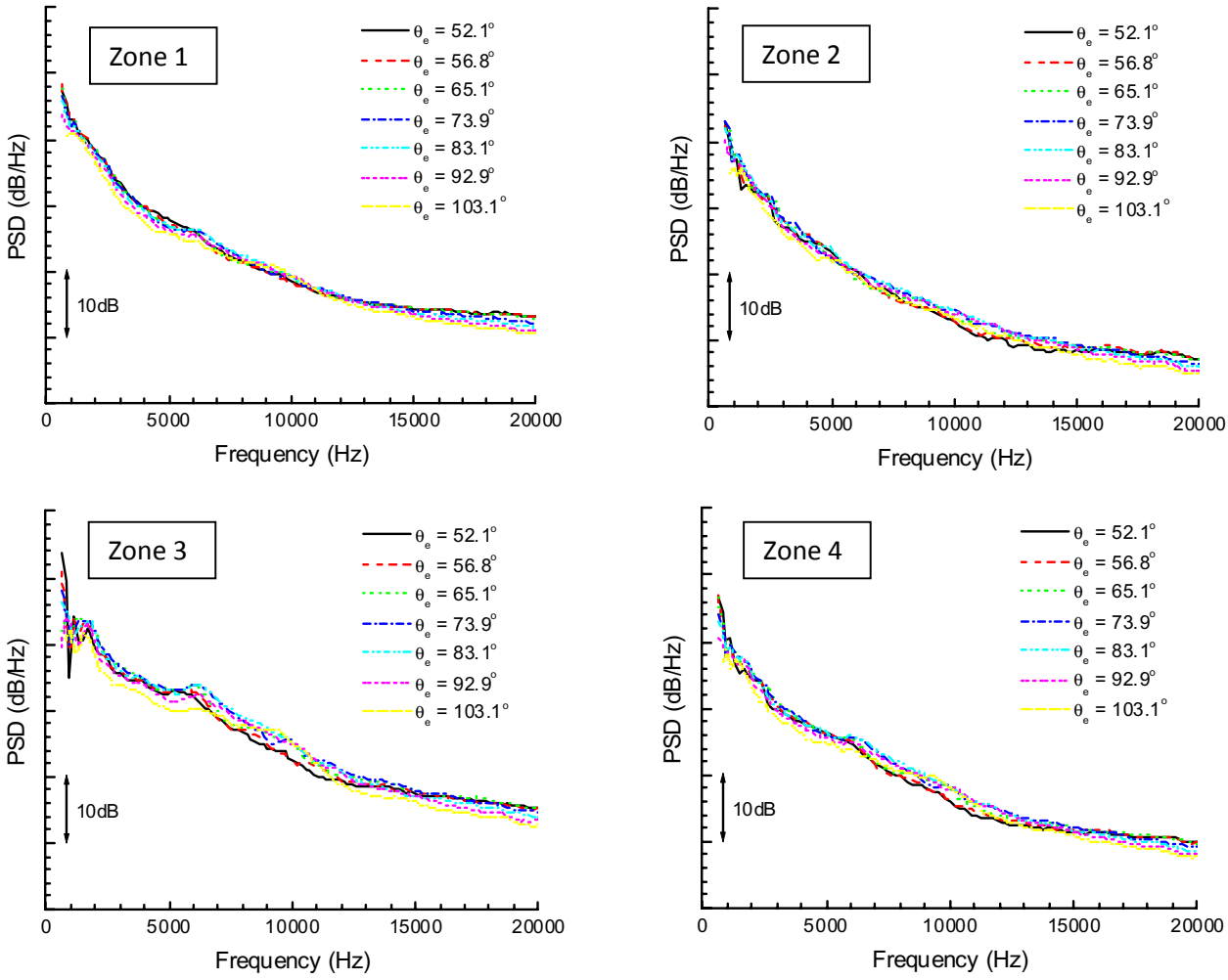

Figure 18. Directivity spectra for zones defined in Fig. 14. Baseline model – no landing gear. Mach 0.2, AoA = 3º, Flap = 39º.

particular combination of array location and pressure sensor, there is very strong coherence displayed between 1 kHz and 4 kHz with a corresponding peak in the COP spectrum. Note that this particular pressure sensor is located very near the trailing edge of the bulb seal cavity on the outboard flap. The induced oscillations both within the cavity and on the upper surface of the flap near the trailing edge of the cavity are strongly radiating and contributing to the displayed coherent signal between the array and pressure sensor. The phase between the array output and the sensor over this frequency range is roughly constant at 100 to 150 degrees but begins to break down above 4 kHz. A detailed analysis of the phase behavior is beyond the scope of the present study, with the main interest being the structures and detail shown in the COP spectral magnitudes.

It is instructive to examine the sum total of the COP spectra for all of the various pressure sensors along the outboard and inboard flap edges in order to view the evolution of the spectra as a function of sensor location. This is shown in Figure 20 for the outboard flap edge, where the various spectra have been stacked for a qualitative comparison (x/c increases from top to bottom in the figure). A clear *COPs* spectral peak occurs at approximately 2 kHz that becomes steadily stronger for those pressure sensors at chord locations where x/c > 0.5 (i.e., sensors P28, P29, and P31). This peak is in agreement with cross-sensor coherence data shown in Ref. 10, Fig. 35. A different trend is observed when the COP spectra are stacked and examined for those pressure sensors along the edge of the inboard flap. This is shown in Figure 21 for the

same test point as in Fig. 20. There is a small peak observed around 1 kHz in the COP spectra for sensor P3, but in general, there is no significant evolution of the spectra observed as one moves along the flap edge, other than a gradual decline in the levels as the frequency increases. This is a somewhat unexpected result, as one would anticipate the COP spectra to reach a maximum for those sensors nearest the location where vortex merging takes place and the pressure fluctuations induced by the rolled up vortex on the top surface of the flap are strongest. This was not observed; furthermore, examination of the COP phase functions for the inboard flap pressure sensors indicate a breakdown of the phase at most frequencies, with corresponding low COP coherence for these sensors. There are three possible explanations for the lack of strong COP coherence along the inboard flap edge. First, cross-sensor coherence data shown in Ref. 10, Fig. 34 indicated that very little coherence was observed between adjacent pressure sensors above 700-800 Hz. Second, it is likely that the microphone array spatial resolution at these low frequencies is not sufficient to yield a suitable COP coherence (i.e., individual unsteady pressure sensor outputs cannot be isolated sufficiently by the array). Third, it is possible that decorrelation of the acoustic waves passing through the 14x22 tunnel open-jet shear layer coupled with tunnel background noise have reduced the coherence between the pressure sensor and array outputs below the ability to detect the coherent output power, even at these lower frequencies. The noise generated by the outboard flap bulb seal cavity occurs across a significantly higher frequency range and exhibits sufficient strength that even with shear layer decorrelation, the coherent output power remains detectable. The broad peak observed in the outboard flap edge integrated spectra in Figs. 15 and 16 is not totally reproduced in the COP spectra. However, it is noted that the cross-sensor coherence observed in Ref. 10, Fig. 35 closely matches in character the COP coherence shown in Fig. 19(b) below 10 kHz. It may be possible to improve the detectability of the COP coherence, and corrections for shear layer decorrelation have been proposed in the literature[24], but were beyond the scope of the present study. Given the observed inconclusive nature of the inboard flap edge COP coherence and spectra, only the COP analysis results for the outboard flap edge sensors are presented subsequently.

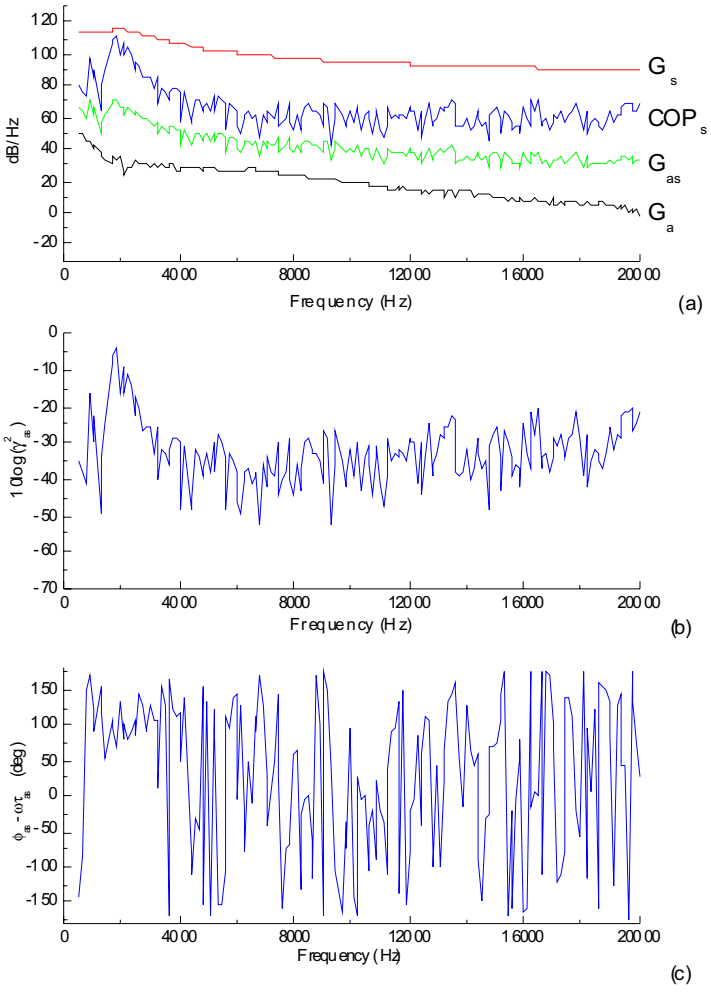

Figure 19. COP analysis example.
Array steered to sensor P31 on outboard flap.
Φ = 100 degrees, θ_e = 92.9 degrees
(a) power spectral densities, (b) coherence, (c) phase

Figures 22 and 23 present the chordwise distributions of integrated band-limited levels from both the unsteady pressure sensor spectra and the COP spectra. The levels are shown along the outboard flap edge using sensors P24, P65, P25, P28, P29, and P31. Note that P24 and P29 were positioned slightly inboard of the remaining sensors at the edge of the flap. The levels shown in the figures result from integrating the

auto-spectra (G_s) for each sensor over a frequency range from 1 to 10.5 kHz. This range was determined empirically via an examination of the band-limited levels computed for a range of bandwidths from 5 to 9.5 kHz for each sensor shown in Fig. 20. It was observed that the 9.5 kHz bandwidth sufficiently captured all of the COP spectral energy of interest. The corresponding integrated *COPs* levels are determined by vectorial summation (over the same frequency range) of the squared-pressure and phase values after adjusting for τ_{as} as shown in Eqn. (9). A total of seven panels are shown in each figure with each panel depicting the noise distributions with the microphone array positioned at each of the polar emission angles in Table 2.

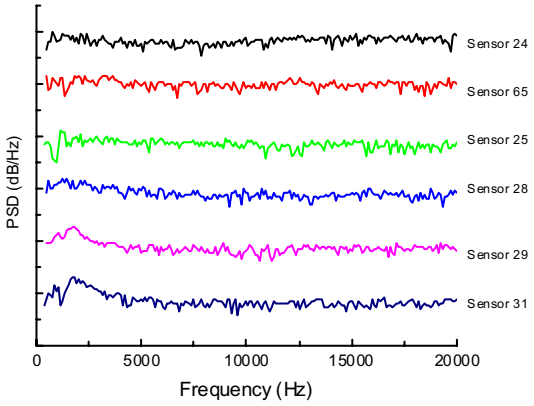

Figure 20. Evolution of *COPs* along outboard flap. Landing gear installed. Φ = 100 degrees, θ_e = 92.9 degrees

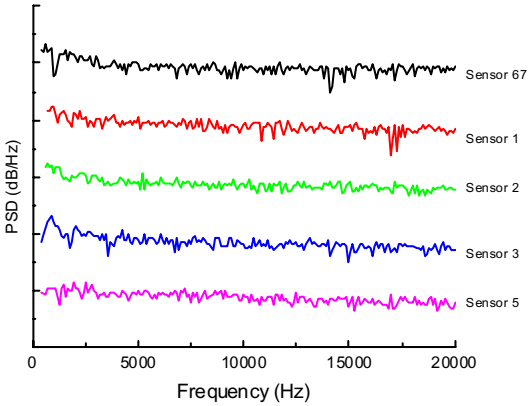

Figure 21. Evolution of *COPs* along inboard flap. Landing gear installed. Φ = 100 degrees, θ_e = 92.9 degrees

In Figs. 22 and 23, it is observed that the integrated auto-spectra for each pressure sensor is almost constant as a function of θ_e. This is expected and is a measure of good repeatability in the sensor outputs. It is also observed that a relative maximum occurs consistently in the vicinity of sensor P65 in the integrated COP spectra. It can be conjectured that this maximum corresponds to a point on the flap (at a chord position x/c = 0.23) near where the initial upper vortex forms before merging with the side vortex. However, the invariance of the peak shown for sensor P65 as a function of θ_e could also be indicative of a problem with that particular sensor's sensitivity or frequency response function. This could not be determined adequately for the present study; however, it was still deemed acceptable to include this sensor in Figs. 22 and 23. Also noted is a clear trend displayed in most of the integrated COP spectra towards a second local maximum in the vicinity of sensor P31 (at a chord position x/c = 0.82) very near the trailing edge of the bulb seal cavity. This again reinforces the conclusion that the bulb seal cavity is one of the predominant sources on the model. All of the trends displayed in Figs. 22 and 23 are relatively insensitive to the landing gear being installed or removed from the model, as would be expected for the outboard flap edge.

IV. Summary

A detailed experimental study of the noise generated by a baseline high-fidelity airframe model was conducted in the open-jet test section of the NASA Langley 14- by 22-foot Subsonic Tunnel on an 18%- scale, semi-span Gulfstream airframe model incorporating a trailing edge flap and main landing gear. Unsteady surface pressure measurements were obtained from a series of sensors positioned along the two flap edges, and far field acoustic measurements were obtained using a 97-microphone phased array that

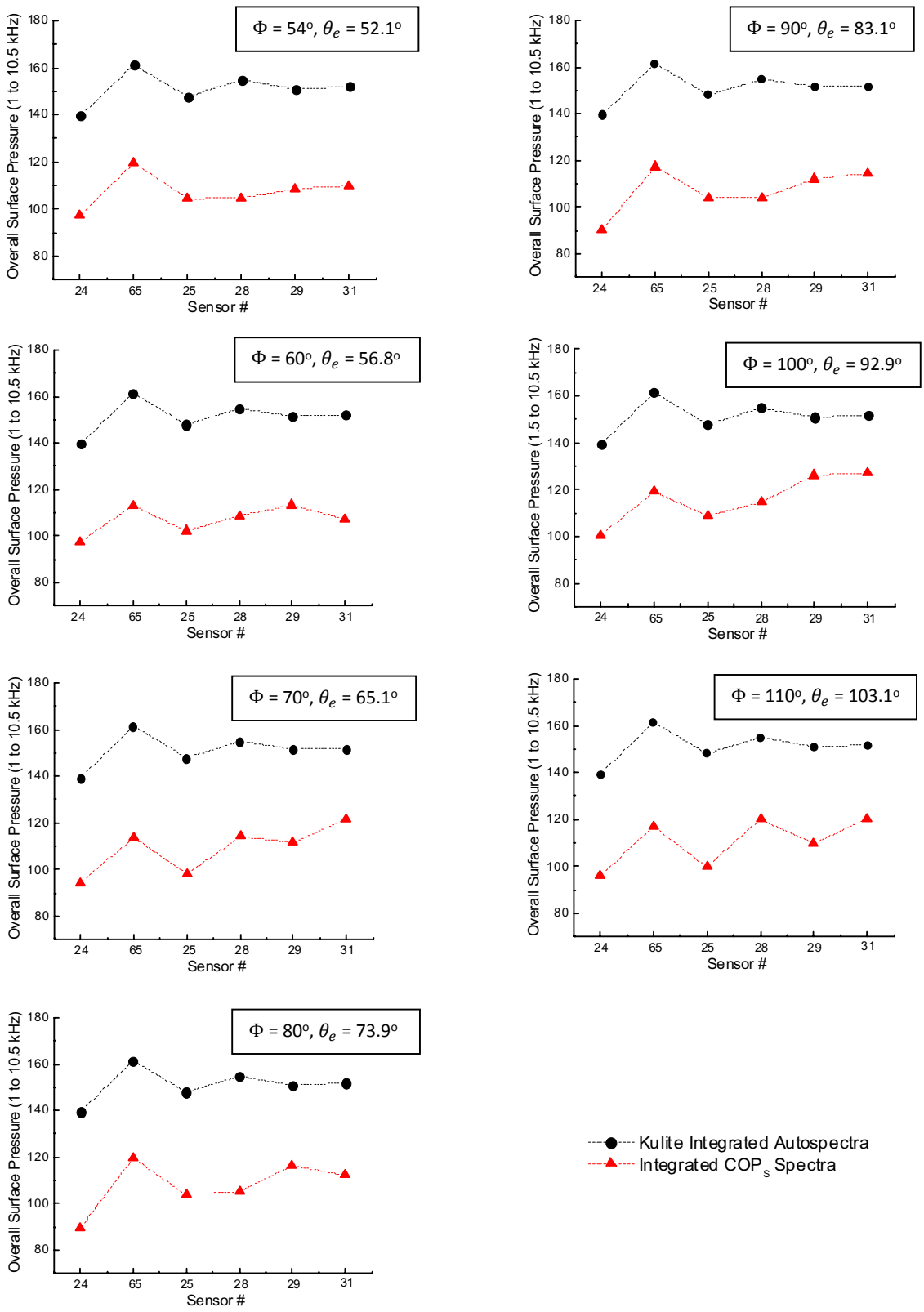

Figure 22. Distribution over outboard flap of band limited overall surface pressure levels and COPs levels. Baseline model with landing gear installed. Mach 0.2, AoA = 3°, Flap = 39°.

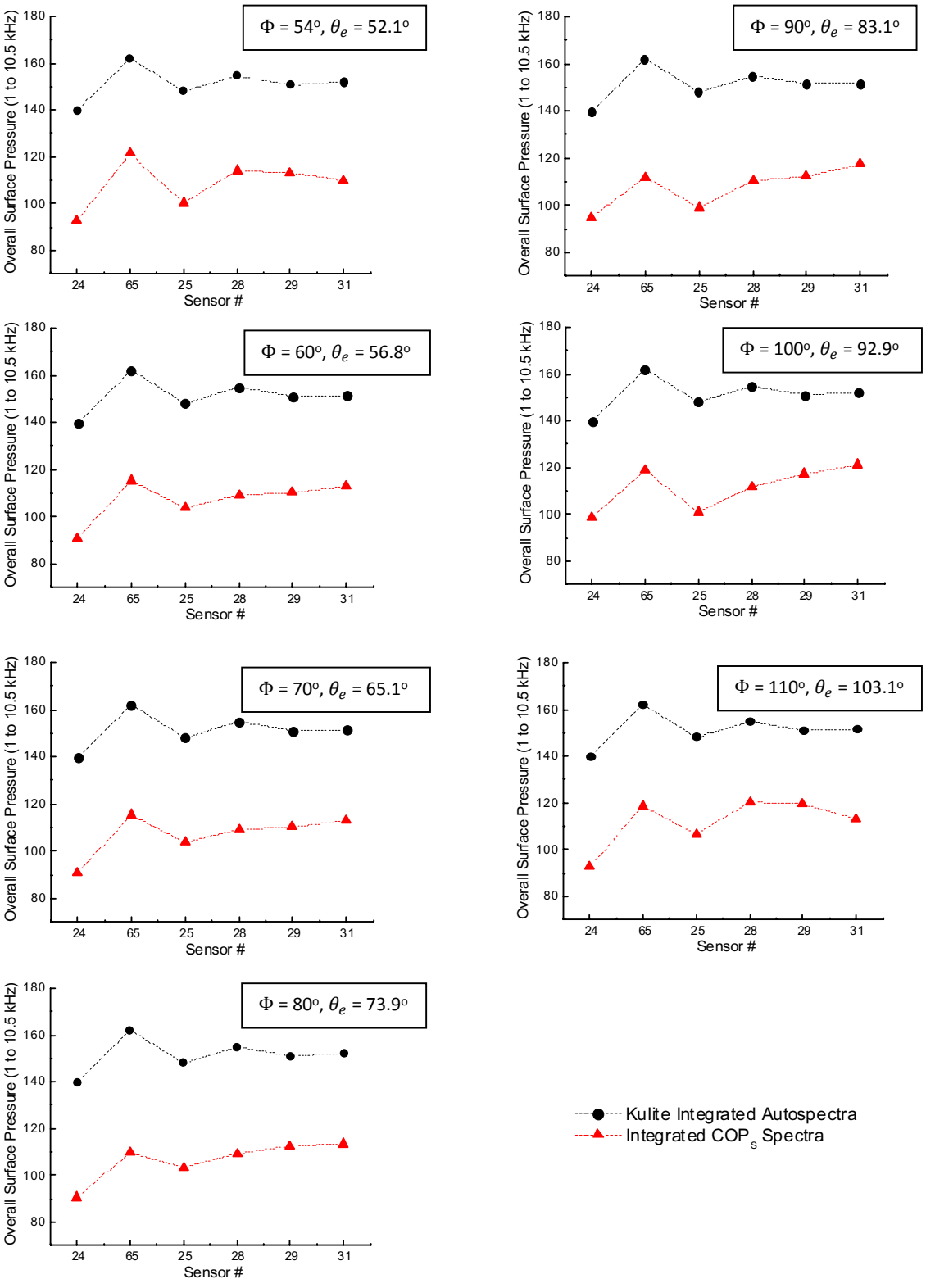

Figure 23. Distribution over outboard flap of band limited overall surface pressure levels and COPs levels. Baseline model – no landing gear. Mach 0.2, AoA = 3°, Flap = 39°.

viewed the pressure side of the airframe. The DAMAS array deconvolution method was employed to determine the locations and strengths of relevant noise sources in the vicinity of the flap edges and the landing gear. A coherent output power spectral method was used to couple the unsteady surface pressures measured along the flap edges with the phased array output. The primary conclusions derived from the study are as follows:

- The outboard flap edge noise was dominated by the bulb seal cavity with very strong COP coherence observed between the array output and those unsteady pressure sensors nearest the aft end of the cavity over an approximate model-scale frequency range of 1 to 5 kHz. This finding was confirmed via generation of integrated band-limited dB levels from the unsteady pressure sensors and COP spectra.
- As shown in the integrated array spectra presented in Figs. 15 and 16, in general the inboard flap generates more far field noise than the outboard flap (with the exception of the noise in the 5-10 kHz range). Unfortunately, an examination of experimental COP spectra for pressure sensors along the inboard flap proved inconclusive at identifying the noise radiation regions along the flap edge, due to the low frequencies involved and possible coherence loss caused by decorrelation of the acoustic waves by the wind tunnel open-jet shear layer coupled with tunnel background noise.
- Removal of the main landing gear on the model had little to no effect on the noise radiation by the outboard flap edge but moderate influence on the noise radiation by the region around the inboard flap edge. The proximity of the inboard flap edge and landing gear made visual separation of noise sources in contour presentations challenging.
- Directivity measurements showed that the flap and landing gear were only moderately directional as a function of polar emission angle.

Future work with the data collected for this study could include the implementation of correction algorithms and methods to counteract shear layer acoustic wave decorrelation and thereby improve the COP coherence between the unsteady pressure sensors and the phased array. Additionally, application of COP methods to the unsteady pressure sensors mounted on the landing gear assembly might yield additional insight into the nature of the noise radiated from the aircraft undercarriage.

Acknowledgments

This work was sponsored by the NASA Environmentally Responsible Aviation (ERA) Project in the Aeronautics Research Mission Directorate.

References

[1]Collier, F. S., "Environmentally Responsible Aviation (ERA) Project," *oral presentation*, NASA Fundamental Aeronautics Program, Third Annual Meeting, Atlanta, GA, Sept., 2009.

[2]Kendal, J. M., and Athye, W. F., "Noise Generation by a Lifting Wing/Flap Combination at Reynolds Number to 2.8 x 10^6," *AIAA Paper 1980-0035*, 18th AIAA Aerospace Sciences Meeting, Pasadena, CA, 1980.

[3]Meadows, K. R., Brooks, T. F., Humphreys, W. M., Hunter, W. W., and Gerhold, C. H., "Aeroacoustic Measurements of a Wing-Flap Configuration," *AIAA Paper 1997-1595*, 3rd AIAA/CEAS Aeroacoustics Conference, Atlanta, GA, 1997.

[4]Radezrsky, R. H., Singer, B. A., and Khorrami, M. R., "Detailed Measurements of a Flap Side-Edge Flow Field," *AIAA Paper 1998-0700*, 36th AIAA Aerospace Sciences Meeting, Reno, NV, 1998.

[5]Khorrami, M. R., and Singer, B. A., "Stability Analysis for Noise-Source Modeling of a Part-Span Flap," *AIAA Journal*, Volume 37 (10), pp. 1206-1212, 1999.

[6]Guo, Y. P., "Prediction of Flap Side Edge Noise," *AIAA Paper 1999-1804*, 5th AIAA/CEAS Aeroacoustics Conference, Bellevue, WA, 1999.

[7]Brooks, T. F., and Humphreys, W. M., "Flap Edge Aeroacoustics: Measurements and Predictions," *Journal of Sound and Vibration*, Volume 261, pp. 31-74, 2003.

[8]Hutcheson, F. V., Brooks, T. F., and Humphreys, W. M., "Noise Radiation from a Continuous Mold-Line Link Flap Configuration," *AIAA Paper 2008-2966*, 14th AIAA/CEAS Aeroacoustics Conference, Vancouver, Canada, 2008.

[9]Khorrami, M. R., Hannon, J. A., Neuhart, D. H., Markowski, G. A., and Van de Ven, T., "Aeroacoustic Study of a High-Fidelity Aircraft Model: Part 1 – Steady Aerodynamic Measurements," *AIAA Paper 2012-2233*, 18th AIAA/CEAS Aeroacoustics Conference, Colorado Springs, CO, 2012.

[10]Khorrami, M. R., and Neuhart, D. H., "Aeroacoustic Study of a High-Fidelity Aircraft Model: Part 2 – Unsteady Surface Pressures," *AIAA Paper 2012-2234*, 18th AIAA/CEAS Aeroacoustics Conference, Colorado Springs, CO, 2012.

[11]Khorrami, M. R., and Mineck, R. E., "Towards Full Aircraft Airframe Noise Prediction: Detached Eddy Simulations," *AIAA Paper 2014-2480*, 20th AIAA/CEAS Aeroacoustics Conference, Atlanta, GA, 2014.

[12]Humphreys, W. M., Brooks, T. F., Bahr, C. J., Spalt, T. B., Bartram, S. M., Culliton, W. G., and Becker, L. E., "Development of a Microphone Phased Array Capability for the Langley 14- by 22-foot Subsonic Tunnel," *AIAA Paper 2014-2343*, 20th AIAA/CEAS Aeroacoustics Conference, Atlanta, GA, 2014.

[13]Hutcheson, F. V., and Brooks, T. F., "Measurement of Trailing Edge Noise Using Directional Array and Coherent Output Power Methods", *AIAA Paper 2002-2472*, 8th AIAA/CEAS Aeroacoustics Conference, Breckenridge, CO, 2002.

[14]Khorrami, M. R., Humphreys, W. M., and Lockard, D. P., "An Assessment of Noise Abatement Concepts for Flap and Main Landing Gear", 21st AIAA/CEAS Aeroacoustics Conference, Dallas, TX, 2015.

[15]Khorrami, M. R., Humphreys, W. M., Lockard, D. P. and Ravetta, P. A., "Aeroacoustic Evaluation of Flap and Landing Gear Noise Reduction Concepts," *AIAA Paper 2014-2478*, 20th AIAA/CEAS Aeroacoustics Conference, Atlanta, GA, 2014.

[16]Neuhart, D. H., Hannon, J. A., and Khorrami, M. R., "Aerodynamic Measurements of a Gulfstream Aircraft Model With and Without Noise Reduction Concepts," *AIAA Paper 2014-2477*, 20th AIAA/CEAS Aeroacoustics Conference, Atlanta, GA, 2014.

[17]Brooks, T. F., Humphreys, W. M., "Effect of Directional Array Size on the Measurement of Airframe Noise Components," *AIAA Paper 1999-1958*, 5th AIAA/CEAS Aeroacoustics Conference, Bellevue, WA, 1999.

[18]NetCDF software and documentation can be found at http://www.unidata.ucar.edu/software/netcdf/.

[19]Bahr, C. J. and Horne, W. C., "Advanced Background Subtraction Applied to Aeroacoustic Wind Tunnel Testing," 21st AIAA/CEAS Aeroacoustics Conference, Dallas, TX, 2015.

[20]Amiet, R. K., "Refraction of Sound by a Shear Layer," *Journal of Sound and Vibration*, Volume 58(3), pp. 467-482, 1978.

[21]Brooks, T. F., and Humphreys, W. M., "A Deconvolution Approach for the Mapping of Acoustic Sources (DAMAS) Determined from Phased Microphone Arrays," *Journal of Sound and Vibration*, Volume 294, pp. 856-879, 2006.

[22]Bendat, J. S., and Piersol, A. G., *Engineering Applications of Correlation and Spectral Analysis*, Wiley, 1980.

[23]Humphreys, W. M., and Brooks, T. F., "Noise Spectra and Directivity for a Scale-Model Landing Gear," *International Journal of Aeroacoustics*, Volume 8(5), pp. 409-444, 2009.

[24]Sijtsma, P., "Acoustic Array Corrections for Coherence Loss Due to the Wind Tunnel Shear Layer," *Berlin Beamforming Conference*, Berlin, Germany, 2008.